Full 3-D OCT-based pseudophakic custom computer eye model

M. Sun,[*] P. Pérez-Merino, E. Martinez-Enriquez, M. Velasco-Ocana, and S. Marcos

Visual Optics & Biophotonics Lab, Instituto de Optica, Consejo Superior de Investigaciones Científicas, Serrano 121, 28006, Madrid, Spain
[*]*mengchan@io.cfmac.csic.es*

Abstract: We compared measured wave aberrations in pseudophakic eyes implanted with aspheric intraocular lenses (IOLs) with simulated aberrations from numerical ray tracing on customized computer eye models, built using quantitative 3-D OCT-based patient-specific ocular geometry. Experimental and simulated aberrations show high correlation (R = 0.93; p<0.0001) and similarity (RMS for high order aberrations discrepancies within 23.58%). This study shows that full OCT-based pseudophakic custom computer eye models allow understanding the relative contribution of optical geometrical and surgically-related factors to image quality, and are an excellent tool for characterizing and improving cataract surgery.

References and links

1. J. S. McLellan, S. Marcos, and S. A. Burns, "Age-related changes in monochromatic wave aberrations of the human eye," Invest. Ophthalmol. Vis. Sci. **42**(6), 1390–1395 (2001).
2. D. A. Atchison, M. J. Collins, C. F. Wildsoet, J. Christensen, and M. D. Waterworth, "Measurement of monochromatic ocular aberrations of human eyes as a function of accommodation by the Howland aberroscope technique," Vision Res. **35**(3), 313–323 (1995).
3. J. C. He, S. A. Burns, and S. Marcos, "Monochromatic aberrations in the accommodated human eye," Vision Res. **40**(1), 41–48 (2000).
4. E. Moreno-Barriuso, J. M. Lloves, S. Marcos, R. Navarro, L. Llorente, and S. Barbero, "Ocular aberrations before and after myopic corneal refractive surgery: LASIK-induced changes measured with laser ray tracing," Invest. Ophthalmol. Vis. Sci. **42**(6), 1396–1403 (2001).
5. S. Barbero, S. Marcos, and I. Jiménez-Alfaro, "Optical aberrations of intraocular lenses measured in vivo and in vitro," J. Opt. Soc. Am. A **20**(10), 1841–1851 (2003).
6. S. Marcos, S. Barbero, and I. Jiménez-Alfaro, "Optical quality and depth-of-field of eyes implanted with spherical and aspheric intraocular lenses," J. Refract. Surg. **21**(3), 223–235 (2005).
7. P. Pérez-Merino, S. Ortiz, N. Alejandre, A. de Castro, I. Jiménez-Alfaro, and S. Marcos, "Ocular and optical coherence tomography-based corneal aberrometry in keratoconic eyes treated by intracorneal ring segments," Am. J. Ophthalmol. **157**(1), 116–127 (2014).
8. T. Olsen, "Calculation of intraocular lens power: a review," Acta Ophthalmol. Scand. **85**(5), 472–485 (2007).
9. J. T. Holladay, P. A. Piers, G. Koranyi, M. van der Mooren, and N. E. Norrby, "A new intraocular lens design to reduce spherical aberration of pseudophakic eyes," J. Refract. Surg. **18**(6), 683–691 (2002).
10. T. Olsen and P. Hoffmann, "C constant: new concept for ray tracing-assisted intraocular lens power calculation," J. Cataract Refract. Surg. **40**(5), 764–773 (2014).
11. M. Saiki, K. Negishi, N. Kato, H. Torii, M. Dogru, and K. Tsubota, "Ray tracing software for intraocular lens power calculation after corneal excimer laser surgery," Jpn. J. Ophthalmol. **58**(3), 276–281 (2014).
12. K. Minami, Y. Kataoka, J. Matsunaga, S. Ohtani, M. Honbou, and K. Miyata, "Ray-tracing intraocular lens power calculation using anterior segment optical coherence tomography measurements," J. Cataract Refract. Surg. **38**(10), 1758–1763 (2012).
13. P. Hoffmann, J. Wahl, and P. R. Preussner, "Accuracy of intraocular lens calculation with ray tracing," J. Refract. Surg. **28**(9), 650–655 (2012).
14. P. Rosales and S. Marcos, "Customized computer models of eyes with intraocular lenses," Opt. Express **15**(5), 2204–2218 (2007).
15. J. Tabernero, P. Piers, A. Benito, M. Redondo, and P. Artal, "Predicting the optical performance of eyes implanted with IOLs to correct spherical aberration," Invest. Ophthalmol. Vis. Sci. **47**(10), 4651–4658 (2006).
16. S. Ortiz, P. Pérez-Merino, S. Durán, M. Velasco-Ocana, J. Birkenfeld, A. de Castro, I. Jiménez-Alfaro, and S. Marcos, "Full OCT anterior segment biometry: an application in cataract surgery," Biomed. Opt. Express **4**(3), 387–396 (2013).

17. S. Ortiz, D. Siedlecki, I. Grulkowski, L. Remon, D. Pascual, M. Wojtkowski, and S. Marcos, "Optical distortion correction in optical coherence tomography for quantitative ocular anterior segment by three-dimensional imaging," Opt. Express **18**(3), 2782–2796 (2010).
18. M. Sun, J. Birkenfeld, A. de Castro, S. Ortiz, and S. Marcos, "OCT 3-D surface topography of isolated human crystalline lenses," Biomed. Opt. Express **5**(10), 3547–3561 (2014).
19. P. Pérez-Merino, M. Velasco-Ocana, E. Martinez-Enriquez, and S. Marcos, "OCT-based crystalline lens topography in accommodating eyes," Biomed. Opt. Express **6**(12), 5039–5054 (2015).
20. S. Ortiz, D. Siedlecki, P. Pérez-Merino, N. Chia, A. de Castro, M. Szkulmowski, M. Wojtkowski, and S. Marcos, "Corneal topography from spectral optical coherence tomography (sOCT)," Biomed. Opt. Express **2**(12), 3232–3247 (2011).
21. M. Sun, A. de Castro, S. Ortiz, P. Perez-Merino, J. Birkenfeld, and S. Marcos, "Intraocular lens alignment from an en face optical coherence tomography image Purkinje-like method," Opt. Eng. **53**(6), 061704 (2014).
22. S. Marcos, S. Ortiz, P. Pérez-Merino, J. Birkenfeld, S. Durán, and I. Jiménez-Alfaro, "Three-dimensional evaluation of accommodating intraocular lens shift and alignment in vivo," Ophthalmology **121**(1), 45–55 (2014).
23. L. Llorente, S. Barbero, D. Cano, C. Dorronsoro, and S. Marcos, "Myopic versus hyperopic eyes: axial length, corneal shape and optical aberrations," J. Vis. **4**(4), 288–298 (2004).
24. I. Grulkowski, M. Gora, M. Szkulmowski, I. Gorczynska, D. Szlag, S. Marcos, A. Kowalczyk, and M. Wojtkowski, "Anterior segment imaging with Spectral OCT system using a high-speed CMOS camera," Opt. Express **17**(6), 4842–4858 (2009).
25. S. Ortiz, D. Siedlecki, L. Remon, and S. Marcos, "Optical coherence tomography for quantitative surface topography," Appl. Opt. **48**(35), 6708–6715 (2009).
26. S. Ortiz, P. Pérez-Merino, N. Alejandre, E. Gambra, I. Jimenez-Alfaro, and S. Marcos, "Quantitative OCT-based corneal topography in keratoconus with intracorneal ring segments," Biomed. Opt. Express **3**(5), 814–824 (2012).
27. S. Ortiz, P. Pérez-Merino, E. Gambra, A. de Castro, and S. Marcos, "In vivo human crystalline lens topography," Biomed. Opt. Express **3**(10), 2471–2488 (2012).
28. M. Sun, A. de Castro, S. Ortiz, P. Perez-Merino, J. Birkenfeld, and S. Marcos, "Intraocular lens alignment from an en face optical coherence tomography image Purkinje-like method," OPTICE **53**(6), 061704 (2014).
29. A. Pérez-Escudero, C. Dorronsoro, and S. Marcos, "Correlation between radius and asphericity in surfaces fitted by conics," J. Opt. Soc. Am. A **27**(7), 1541–1548 (2010).
30. D. R. Iskander, "Computational aspects of the visual Strehl ratio," Optom. Vis. Sci. **83**(1), 57–59 (2006).
31. L. Llorente, L. Diaz-Santana, D. Lara-Saucedo, and S. Marcos, "Aberrations of the human eye in visible and near infrared illumination," Optom. Vis. Sci. **80**(1), 26–35 (2003).
32. L. N. Thibos, R. A. Applegate, J. T. Schwiegerling, and R. Webb; VSIA Standards Taskforce Members. Vision science and its applications, "Standards for reporting the optical aberrations of eyes," J. Refract. Surg. **18**(5), S652–S660 (2002).
33. P. Rosales, M. Wendt, S. Marcos, and A. Glasser, "Changes in crystalline lens radii of curvature and lens tilt and decentration during dynamic accommodation in rhesus monkeys," J. Vis. **8**(1), 18 (2008).
34. S. Marcos, P. Rosales, L. Llorente, S. Barbero, and I. Jiménez-Alfaro, "Balance of corneal horizontal coma by internal optics in eyes with intraocular artificial lenses: evidence of a passive mechanism," Vision Res. **48**(1), 70–79 (2008).
35. P. Pérez-Merino, C. Dorronsoro, L. Llorente, S. Durán, I. Jiménez-Alfaro, and S. Marcos, "In vivo chromatic aberration in eyes implanted with intraocular lenses," Invest. Ophthalmol. Vis. Sci. **54**(4), 2654–2661 (2013).
36. M. Vinas, C. Dorronsoro, D. Cortes, D. Pascual, and S. Marcos, "Longitudinal chromatic aberration of the human eye in the visible and near infrared from wavefront sensing, double-pass and psychophysics," Biomed. Opt. Express **6**(3), 948–962 (2015).
37. J. Birkenfeld, A. de Castro, and S. Marcos, "Contribution of shape and gradient refractive index to the spherical aberration of isolated human lenses," Invest. Ophthalmol. Vis. Sci. **55**(4), 2599–2607 (2014).
38. A. de Castro, J. Birkenfeld, B. Maceo, F. Manns, E. Arrieta, J. M. Parel, and S. Marcos, "Influence of shape and gradient refractive index in the accommodative changes of spherical aberration in nonhuman primate crystalline lenses," Invest. Ophthalmol. Vis. Sci. **54**(9), 6197–6207 (2013).
39. I. Grulkowski, J. J. Liu, B. Potsaid, V. Jayaraman, C. D. Lu, J. Jiang, A. E. Cable, J. S. Duker, and J. G. Fujimoto, "Retinal, anterior segment and full eye imaging using ultrahigh speed swept source OCT with vertical-cavity surface emitting lasers," Biomed. Opt. Express **3**(11), 2733–2751 (2012).
40. M. Ruggeri, S. R. Uhlhorn, C. De Freitas, A. Ho, F. Manns, and J. M. Parel, "Imaging and full-length biometry of the eye during accommodation using spectral domain OCT with an optical switch," Biomed. Opt. Express **3**(7), 1506–1520 (2012).
41. M. C. Dunne, J. M. Royston, and D. A. Barnes, "Posterior corneal surface toricity and total corneal astigmatism," Optom. Vis. Sci. **68**(9), 708–710 (1991).
42. M. Dubbelman, V. A. Sicam, and G. L. Van der Heijde, "The shape of the anterior and posterior surface of the aging human cornea," Vision Res. **46**(6-7), 993–1001 (2006).
43. K. Kamiya, K. Shimizu, M. Yamagishi, A. Igarashi, and H. Kobashi, "Anterior and Posterior Corneal Astigmatism after Refractive Lenticule Extraction for Myopic Astigmatism," J. Ophthalmol. **2015**, 915853 (2015).
44. J. Birkenfeld, A. de Castro, S. Ortiz, D. Pascual, and S. Marcos, "Contribution of the gradient refractive index and shape to the crystalline lens spherical aberration and astigmatism," Vision Res. **86**, 27–34 (2013).

45. S. Marcos, P. Rosales, L. Llorente, and I. Jiménez-Alfaro, "Change in corneal aberrations after cataract surgery with 2 types of aspherical intraocular lenses," J. Cataract Refract. Surg. **33**(2), 217–226 (2007).

1. Introduction

Ocular aberrometry has become a standard tool in research and in the clinic to measure the optical quality of the eye, and its changes with aging [1], accommodation [2, 3] and with surgical interventions (i.e. LASIK [4], intraocular lens (IOL) implantation surgery [5, 6], keratoconus and Intracorneal Ring Segment (ICRS) implantation [7], etc...). Furthermore, new refractive produces and, more specifically, the availability of a large number of IOL options hold promise for a customized intervention, adapted to the patient's needs. There is an increasing number of IOLs available aiming at modifying the patient's wave aberrations, targeting correction of both refractive error and some high order aberrations (i.e. spherical aberration, such as in aspheric designs, or aiming at the increase of depth-of-focus in presbyopic-correction IOLs). However, these efforts have not in general been paralleled by a sophistication of the methods to select the most suitable IOL, or to predict the optical quality outcomes. Generally, the methods to calculate the power of the IOL to be implanted are based on paraxial regression formulae, based on population averages [8]. Furthermore, simulations of the optical performance of new IOL designs either generally assume diffraction-limited optics in the eye, or simple eye models [9] that are based on average anatomic data across the population and numerous simplifications (i.e. centered optics rotationally, symmetric optical surfaces, etc...). The suitability of custom eye models to improve the predictability of cataract surgery has been acknowledged. Several authors have presented the use of non-paraxial eye models for improved selection of the IOL to be implanted, in particular, for the calculation of IOL power with higher accuracy than regression-formulae [10–13]. Customized eye models have also been shown to accurately reproduce measured high order aberrations, when constructed using the anatomical parameters of individual patients [14, 15]. These models are instrumental in understanding the relative contribution of the patient's corneal topography, IOL design, IOL tilt and decentration, and foveal misalignment, and as platforms to test what optical performance would have resulted if the eye had been implanted with a different IOL design. Typically, the anatomical parameters of the eye to build these eye models are obtained from various instruments (Placido Disk corneal elevation maps; Purkinje imaging IOL tilt, decentration and foveal position, IOL design provided by the manufacturer) [14, 15]. Recently, quantitative OCT imaging has shown to be a powerful technology to obtain quantitative 3D optical biometry and geometry in individual eyes [16], providing, from a single instrument, all the ocular anterior segment information needed to build a custom pseudophakic model eye.

Quantitative OCT anterior segment imaging requires correction of fan distortion (arising from the scanning architecture) and optical distortion (due to the refraction in the optical surfaces) [17], as well as dedicated image processing routines [16]. The technique has demonstrated to provide accurate corneal topographies, crystalline lens topographies [18–20], 3D optical biometry pre- and post-operative cataract surgery [16] and tilt and decentration of IOL and/or crystalline lens [21]. In addition, previous work has shown that ray tracing through OCT-based corneal topographies allows computation of corneal aberrometry, showing high degrees of agreement with total aberrometry in a group keratoconic eyes pre- and post- implantation of intrastromal corneal ring segments [7]. Also, 3D biometric quantitative anterior segment OCT in patients with accommodating IOLs [22] shows good correspondence with certain aberration terms measured on the same eyes: i.e. the observed axial shifts with accommodative demand are in good agreement with the measured shifts in defocus, or the increased amounts of IOL tilt with the measured increased coma [22].

In this work we present a customized model eye fully based on OCT 3D geometrical data in patients implanted with IOLs. Comparison of the geometry of IOL *ex vivo* samples to the IOL geometry measured *in vivo* will serve as additional further support of the quantitative potential of the 3D anterior segment OCT. Experimental measurements of ocular aberrations on these eyes will be compared with estimates of ocular aberrations

from numerical ray tracing using a customized model eye from individual OCT measurements of post-operative corneal topography, anterior chamber depth, IOL geometry, IOL tilt and decentration and foveal misalignment. This study will allow validation of the accuracy of OCT-based customized eye models to predict measured aberrations, and to investigate the contribution of the different components to overall image quality in eyes with IOLs, thus demonstrating the capability of quantitative 3D anterior segment OCT to estimate optical aberrations, and its potential to assess post-operative optical quality in pseudophakic eyes. These validations will be a first step into investigating the potential for OCT-based model eyes to become the reference for ray tracing based IOL selection (pre-operatively) and to understand mechanisms of operation and optical outcomes of premium IOLs.

2. Methods

2.1. Patient, surgery and measurements

Three eyes (2, OS; 1, OD) of two patients (64 and 78 years old) implanted with IOLs from two different manufacturers (Akreos AO M160, Bausch and Lomb, Rochester, New York, US; CT Asphina 409M, Zeiss, Jena, Germany) were measured three months after cataract surgery. Standard phaco-emulsification intracapsular cataract surgery had been performed by a single surgeon at Fundación Jiménez Díaz Hospital (FJD) with 2-mm corneal incisions (temporal in OD and nasal in OS). Table 1 shows the patients' clinical profile and details on the implanted IOLs. Total wave aberrations were measured using a custom-developed Laser Ray Tracing (LRT) system [23]. Anterior segment geometry (cornea, iris and IOL) was measured using a custom-developed spectral Optical Coherence Tomography (OCT) [24]. Measurements were done under mydriasis (2.5% phenylephrine). LRT measurements were done under foveal fixation, and OCT measurements were done at the off-axis fixation that aligns the pupillary axis with the optical axis of the instrument. Experimental protocols were approved by Institutional Review Boards at FJD and CSIC. Patients signed informed consent after the nature of the study had been explained to them. All protocols followed the tenets of the Declaration of Helsinki.

Table 1. Patients' clinical profile and details on the implanted IOLs

Subject	Male/ Female	Age	Lens implanted	ACD (mm)	AL (mm)	IOL Power	Post-op Spherical Error	Post-op Cylinder/axis
S1-OD	Male	78	Akreos,Bausch+Lomb	4.31±0.02	23.35	20D	-0.50	-1.75 / 100
S2-OS	Female	64	Asphina IOL,Zeiss	3.80±0.01	23.08	20.5D	+0.25	-1.00 / 85
S3-OS	Male	78	Akreos,Bausch+Lomb	4.48±0.02	23.28	21.5D	+1.25	-1.25 / 90

2.2. 3D anterior segment optical coherence tomography (OCT)

Briefly, the spectral OCT set-up [24] is based on a fiber-optics Michelson interferometer configuration with a superluminescent diode ($\lambda 0 = 840$ nm, $\Delta\lambda = 50$ nm) as a light source and a spectrometer consisting of a volume diffraction grating, and a CMOS camera as a detector. The effective acquisition speed is 25000 A-Scans/s. The axial resolution given by the coherence length of the OCT is 6.9 µm. The axial range is 7 mm in depth, resulting in a theoretical pixel resolution of 3.4 µm. Measurements were collected in a 10 x 10 mm area, and consisted of a collection of 50 B-scans composed by 300 A-scans. This aspect was analyzed in depth in a previous study, where we measured consecutively the cornea with decreasing acquisition times (from 2.0 s to 0.5 s) and found that measurements below 0.8 seconds were stable, preventing the need for applying motion distortion artifacts that we developed for that matter, in most cases [20]. In this study, we used a 0.6 s acquisition speed in a dense, regular and homogeneous sampling which was deemed to provide an appropriate balance between resolution and speed for repetitive measurements and did not require the implementation of motion compensation by software [20].

Measurements were obtained while the subject fixates on a minidisplay that projects a 20/20 Snellen E-letter stimulus. A Badal system compensates for the spherical error of the

patient. The stimulus is moved across the display to change the eye's fixation angle, so that the optical axis of the instrument is aligned with the pupillary axis [19]. For foveal fixation the iris appears asymmetrically tilted (Fig. 1(a)), whereas for the selected fixation the iris appears flat (Fig. 1(b)) in the continuous horizontal and vertical cross-sectional views of the anterior segment used during alignment. The off-axis position of the fovea (angle lambda, λ) is calculated from the eye rotation between both alignments. Sets of 3D images of the anterior segment were captured approximately 5 seconds after blinking.

(a)   (b)   (c)
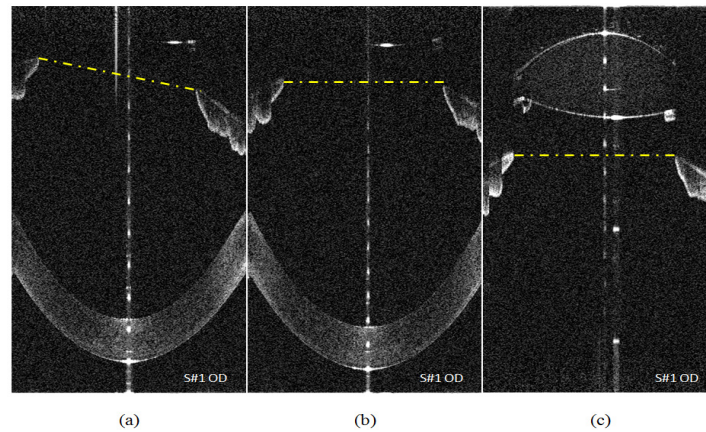
Fig. 1. Acquisition at two different foci (cornea and lens) (a) Vertical cross-sectional scans of a patient's cornea while fixating foveally, i.e. along the line of sight; (b) Vertical cross-sectional scans of a patient's cornea, while fixating eccentrically, i.e. pupilary axis aligned with the OCT optical axis (c) Vertical cross-sectional scans of the IOL implanted in patient. Typical image acquisitions are obtained with the alignment as in (b) and (c). The yellow line indicates the iris plane, used for merging. Images are for subject S1#OD.

The system is provided with fan and optical distortion correction, which compensates for the distortions produced by the scanning architecture of the instrument [25] and the distortion produced by the refraction from the preceding optical surfaces [17, 26, 27]. The automatic image processing tools for denoising, segmentation, clustering, merging, and biometric and IOL alignment measurements have been described in detail before [16, 19]. The quantification capabilities of the instrument have been demonstrated with artificial model eyes with known dimensions, *ex vivo* and *in vivo* measurements, and comparisons with other instruments (videokeratoscopy, Scheimpflug, Purkinje imaging, and non-contact profilometry) [14, 27, 28].

Anterior and posterior corneal elevation maps, corneal thickness, and anterior chamber depth were obtained from 3D OCT as described in earlier publications [19]. Anterior and posterior corneal elevation maps were fit by 6th order Zernike polynomials. For comparison, anterior and posterior corneal topographies were also obtained from Pentacam Scheimpflug topographer (Oculus, Inc., Lynnwood, WA). IOL tilt and decentration was obtained using the OCT-based method described by Sun et al. [21].

2.3. Ex vivo IOL geometry: non-contact profilometry

The geometry of the IOLs (Akreos 20D, 21.5D, Bausch + Lomb; Asphina 20.5D, Zeiss) was characterized *ex vivo* using microscopy-based noncontact profilometry (Sensofar, PLu2300, Barcelona, Spain) with 0.1-μm nominal vertical precision (on rigid samples). De-hydration effects on these IOLs with high water content (25-26%) decrease the effective precision. Repeated measurements on these lenses revealed repeatability in the apex measurement of 5 μm. Both anterior and posterior lens surface topographies were measured in a 5.5x5.5 mm range (50x50 points, 0.11 mm steps). The IOL surface profiles were fitted by conics [29].

2.4. Customized eye models

OCT-based elevation data from both anterior and posterior corneal surfaces, anterior segment distances, IOL geometry and alignment data, angle lambda, and axial length from IOLMaster (Carl Zeiss AG, Jena, Germany) were exported to ZEMAX (Radiant ZEMAX; Focus software, Tucson, AZ, USA), where the custom model eyes were built. Refractive indices of cornea, aqueous humour, vitreous humour, Akreos IOLs and Asphina IOLs were 1.376, 1.337, 1.337, 1.458 and 1.460 respectively, at 555nm.

Wave aberrations were calculated in the pupil plane by tracing an array of 64x64 collimated rays through the eye surfaces within a central 5-mm pupil diameter area, at 555 nm. Figure 2 illustrates the computation of aberrations from OCT data, i.e. ray tracing calculation on OCT distortion-corrected corneal and IOL surfaces. Data are analyzed in terms of Zernike terms and retinal image quality metrics (MTF and Visual Strehl [30]).
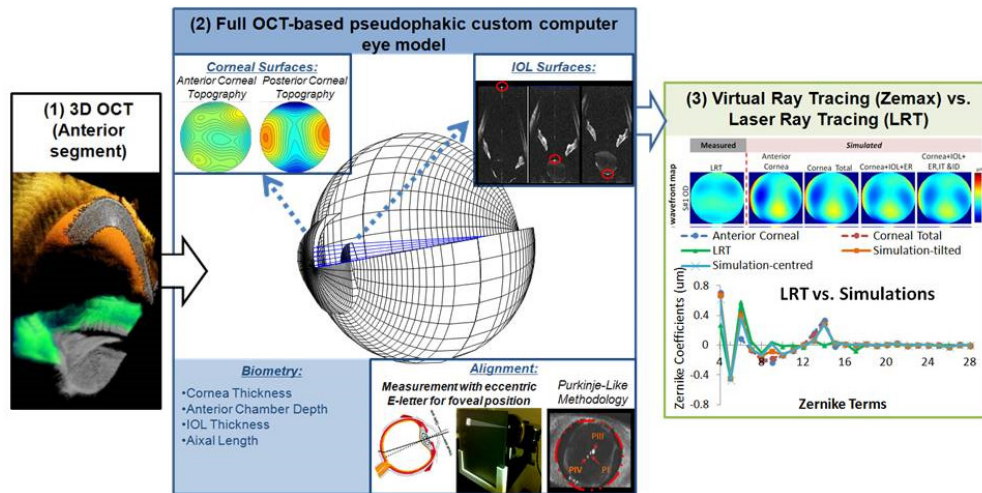
Fig. 2. Illustration of the computation of aberrations using quantitative OCT geometrical data in a customized computer pseudophakic eye model.

2.5. Total aberration measurements: laser ray tracing (LRT)

Total wave aberrations were measured using custom Laser Ray Tracing, described in detail in a previous study [31]. In brief, an infrared (785-nm) laser beam sampled 37 positions across the pupil sequentially in a hexagonal sampling pattern while a charge-couple device (CCD) camera recorded the corresponding aerial images of light reflected off the retina. The sampling pattern was adjusted by software to fit a 5-mm pupil centered at the pupil center. Prior to the measurement, the patient adjusted his/her subjective refraction using a Badal optometer, while viewing a stimulus on a minidisplay placed on a retinal conjugate plane. Ray aberrations were obtained by estimating the deviations of the centroids of the retinal spots images corresponding to each entry pupil location with respect to the reference (chief ray). These deviations are proportional to the local derivatives of the wave aberrations. Maximum energy exposure was 6.8 μW. All measurements were done under foveal fixation of a Maltese cross. Wave aberrations were fitted by 6th order Zernike polynomial expansions, with ordering and normalization following OSA standards [32]. Computations of the Modulation Transfer Function from the wave aberrations were performed using standard Fourier Optics. Root Mean Square (RMS) wavefront error and the MTF were used as optical quality metrics.

3. Results

3.1. OCT-based anterior segment geometry in pseudophakic eyes

Table 2 shows anterior and posterior corneal shape (radii of curvature calculated from the best-fit sphere over 6-mm diameter and some relevant Zernike terms from the polynomial fitting to the corneal elevation maps) and biometry (3D OCT Corneal thickness, and Anterior Chamber Depth).

Table 2. Individual OCT-based biometrical and geometrical data used in the computer model eyes. Data are shown as average ± standard deviation of repeated measurements

	S#1 OD	S#2 OS	S#3 OS
Anterior corneal radius (mm)*	7.74±0.16	7.67±0.19	7.77±0.18
Anterior corneal elevation selected Zernike values (µm)*:	Z_2^2 : 119.6±58.9	Z_2^2 : 120.5±60.5	Z_2^2 : 118.4±59.2
	Z_2^{-2} : 1.48±0.05	Z_2^{-2} : 1.10±0.14	Z_2^{-2} : 1.35±0.33
	Z_3^1 : 0.21±0.07	Z_3^1 : 0.42±0.69	Z_3^1 : 0.13±0.35
	Z_3^{-1} : -0.33±0.68	Z_3^{-1} : 0.40±0.11	Z_3^{-1} : -0.12±0.19
	Z_3^3 : -0.36±0.19	Z_3^3 : -0.37±0.18	Z_3^3 : -0.13±0.01
	Z_3^{-3} : -0.04±0.12	Z_3^{-3} : -0.71±0.36	Z_3^{-3} : 0.13±0.13
	Z_4^0 : 0.93±0.88	Z_4^0 : 0.74±0.32	Z_4^0 : 0.65±0.97
Posterior corneal radius (mm)*	6.28±0.14	6.18±0.13	6.36±0.13
Posterior corneal elevation selected Zernike values (µm)*:	Z_2^2 : 147.2±71.2	Z_2^2 : 151.6±77.9	Z_2^2 : 147.2±73.6
	Z_2^{-2} : -10.85±1.33	Z_2^{-2} : -5.42±2.04	Z_2^{-2} : -9.80±0.01
	Z_3^1 : -0.13±0.59	Z_3^1 : 0.21±0.60	Z_3^1 : 0.46±0.97
	Z_3^{-1} : 0.36±1.31	Z_3^{-1} : 1.00±1.19	Z_3^{-1} : -0.66±1.64
	Z_3^3 : -0.30±0.50	Z_3^3 : 0.22±0.23	Z_3^3 : -0.01±0.81
	Z_3^{-3} : 0.40±0.67	Z_3^{-3} : -0.64±0.13	Z_3^{-3} : -1.20±0.24
	Z_4^0 : 1.00±0.07	Z_4^0 : 2.80±1.32	Z_4^0 : 0.70±0.59
Corneal Thickness (mm)	0.53±0.01	0.57±0.01	0.53±0.01
ACD (mm)	4.31±0.02	3.80±0.01	4.48±0.02
IOL thickness (mm)	0.91±0.01	1.01±0.01	0.85±0.05

* from the corresponding best-fitting sphere

Figure 3 shows OCT-based anterior and posterior corneal elevation maps in all 3 eyes, centered at the pupil center, and for 6-mm pupil diameters. For comparison, corneal maps from Pentacam obtained on the same eyes using the same pupil reference and analysis are also shown. The RMS difference in corneal elevation between instruments is less than 0.04 mm and 0.06 mm, for anterior and posterior surfaces, respectively. In all eyes, astigmatism appears to be the dominant term in the posterior corneal maps, with 19.6% average difference in magnitude and 6.5 deg difference in axis between OCT and Pentacam topographies.
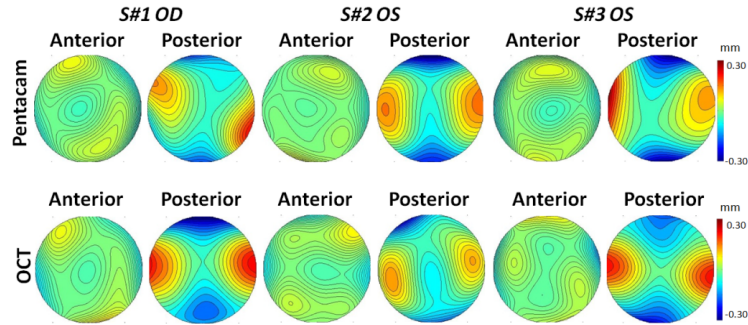
Fig. 3. Anterior and posterior corneal topographic maps from Pentacam (upper panel) and OCT (lower panel). OCT-based maps were used in the computer eye models. Data are for 6-mm pupil.

Table 3 shows measurements of eye rotation, and IOL tilt and decentration (horizontal and vertical components) for each eye. The tilt and decentration nomenclature and sign conventions correspond to those published in prior publications (for an illustration of the convention see Fig. 7 in Rosales et al. 2008 [33]).

Table 3. Eye rotation and IOL tilt and decentration data from OCT-based Purkinje-like methods. Data are average ± standard deviation of 5 repeated measurements. Rotation/tilt X stands for rotation/tilt around the horizontal axis; Rotation/tilt Y stands for rotation/tilt around the vertical axis. Decentration X/Y stands for horizontal /vertical decentration.

Visual axis	S#1 OD	S#2 OS	S#3 OS
Eye rotation X (degree)	-1.33±0.46	-1.83±0.38	-0.14±0.27
Eye rotation Y (degree)	4.13±0.21	-3.55±0.58	-2.43±0.78
IOL tilt X (degree)	-2.22±0.49	1.07±0.41	-2.46±0.26
IOL tilt Y (degree)	-0.26±0.39	-1.75±0.85	-1.20±0.35
IOL decentration X (mm)	0.01±0.06	-0.61±0.05	0.05±0.02
IOL decentration Y (mm)	-0.12±0.19	0.19±0.16	-0.32±0.14

3.2 Comparing OCT-based IOL geometry in vivo with profilometry ex vivo

Comparison of the IOL geometry measured *in vivo* (OCT) and *ex vivo* (non-contact profilometry) serves as a further validation of the accuracy of the OCT (provided with distortion correction algorithms and analysis tools). Table 4 compares the radii of curvature and asphericity values for anterior and posterior IOL surfaces from profilometry and OCT, and the estimated IOL power from these values, compared to the nominal IOL power. The mean differences between the radii of curvature measured by profilometry *ex vivo* and OCT *in vivo* are 0.40 ± 0.28 mm (96.83% agreement), and for the asphericity 2.17 ± 1.64 (17.96%). The geometrical differences between techniques result in less than 0.44 D difference between the IOL power estimated from profilometry and OCT, and less than 0.22 D between the OCT based IOL power estimates *in vivo* and the nominal IOL power.

Table 4. Anterior and posterior radius of curvature (R), asphericity (Q) from profilometry and OCT, and the IOL power estimated from profilometry and OCT. OCT-based data were used in the computer eye models.

		S#1 OD		S#2 OS		S#3 OS	
		R (mm)	Q	R (mm)	Q	R (mm)	Q
Anterior	Profilometry	10.55±0.06	-0.03±0.11	11.90±0.17	-0.24±0.05	10.00±0.28	-0.3±0.11
IOL	*OCT*	*11.00±0.10*	*-4.56±0.08*	*11.51±0.11*	*-2.63±1.62*	*10.05±0.18*	*-1.44±0.23*
Posterior	Profilometry	13.53±0.5	-1.09±0.14	12.90±1.92	-0.5±0.64	12.80±3.01	-0.4±0.11
IOL	*OCT*	*14.2±0.05*	*-0.05±0.40*	*12.17±3.9*	*00.8±0.41*	*12.9±0.33*	*-3.99±0.80*
IOL	*Nominal*	20 D		20.5D		21.5D	
	Profilometry	20.4 D		20.8 D		21.7D	
Power	*OCT*	19.9 D		20.8 D		21.8D	

3.3 Ocular aberrations: laser ray tracing, vs. computer ray tracing on custom model eye

Figure 4 shows examples of measured (first column) and simulated (column 2-5) wave aberrations in three subjects (S#1 OD, S#2 OS, and S#3 OS) for (a) 2nd and higher order aberrations excluding tilt and defocus and (b) for 3rd and higher order aberrations, for 5-mm pupil diameters. Anterior cornea stands for wave aberration of the eye with only the anterior corneal surface; Cornea total stands for the wave aberration of the eye with a 2-surface cornea, without the IOL; Cornea + IOL stands for the wave aberration of the eye with the IOL assuming that the IOL is perfectly aligned with respect to the pupillary axis; Corneal + rot/dec IOL stands for the wave aberration of the eye with the IOL tilted and decentered according to the measured tilts and decentrations.
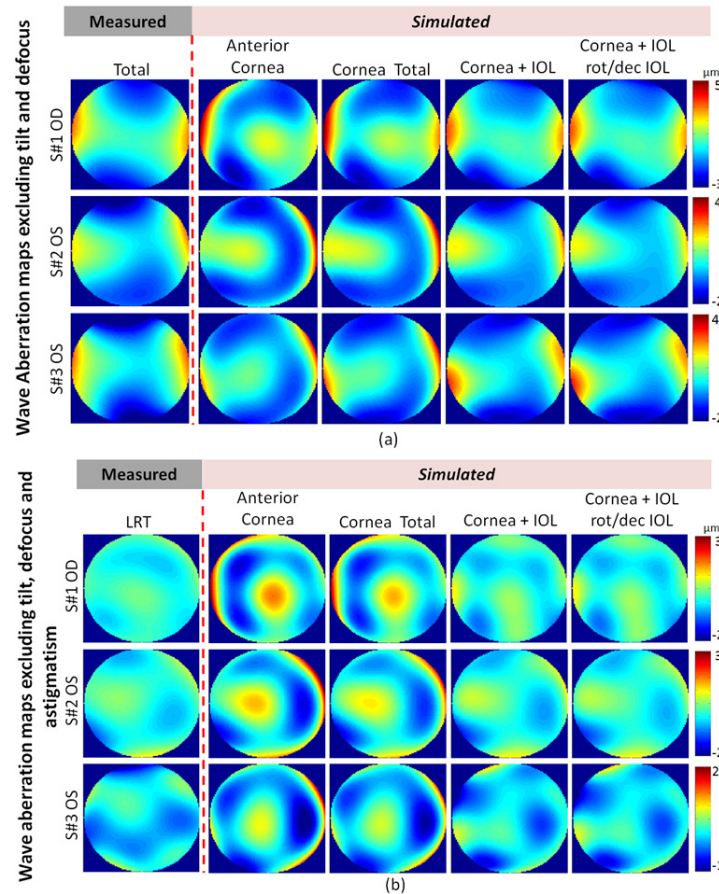
Fig. 4. Measured (LRT, 1st column) and Simulated (from OCT-based geometry/biometry, 2nd −5th columns) wave aberration maps in three pseudophakic Simulated aberrations include wave aberration maps for the anterior cornea alone (2nd column); anterior and posterior cornea (3rd column); eye wave aberration with IOL assuming no tilt and decentration (4th column); eye wave aberration with IOL with no tilt/decentration (5th column). (a) Wave aberration maps including astigmatism (no tilt or defocus); (b) Wave aberrations for 3rd and higher order; Data are for 5-mm pupil, and for foveal fixation, i.e. including eye rotation.

The eyes are rotated according to angle λ in order to incorporate the line-of-sight misalignment. In general, the corneal wave aberration map shows many of the relevant features of the measured wave aberrations.

Figure 5 compares RMS wavefront error for different Zernike orders and terms for the LRT-measured eye aberrations, for the cornea (anterior only or total cornea), for the total eye assuming that the IOL is centered, and for the total eye with the real tilt and decentration with measured total aberrations. The discrepancy between the measured and real aberrations is less than 14.33% (0.15 µm) for astigmatism, and less than 21.43% (0.03 µm) for spherical aberration. In contrast, the larger differences occur for trefoil (in Subjects 1 and 3), coma (in Subject 3) and tetrafoil (in all Subjects). On average, the discrepancies for RMS for astigmatism and higher order aberrations and RMS for high order aberrations alone are 0.12 µm and 0.08 µm, respectively.
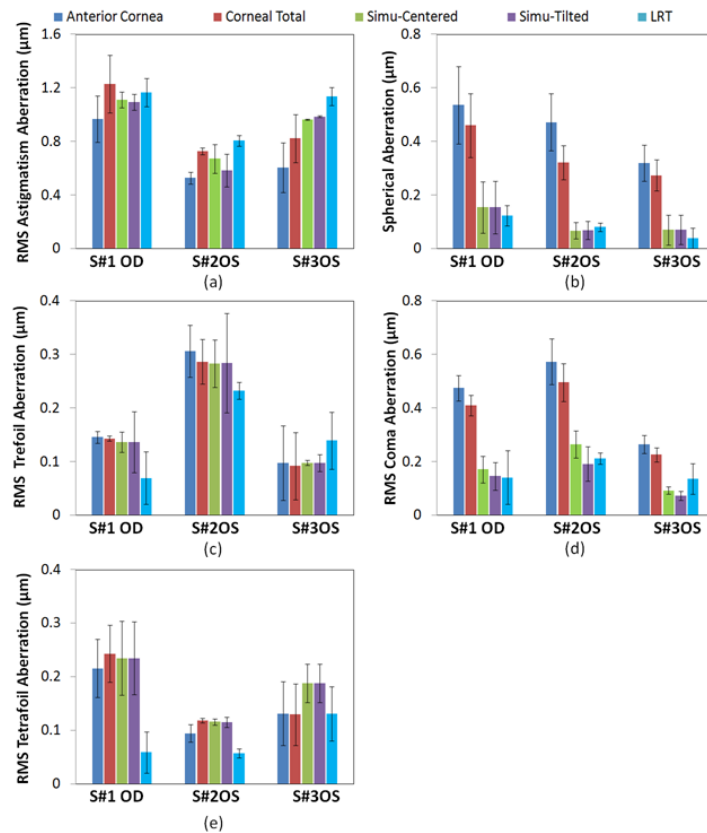
Fig. 5. (a) RMS Astigmatism; (b) RMS Spherical Aberration; (c) RMS Trefoil; (d) RMS Coma; (e) RMS Tetrafoil, for anterior corneal RMS (blue bars), total corneal RMS (red bars), simulated total eye RMS assuming centered IOL (green bars), simulated total eye RMS assuming real IOL tilt/decentration (purple bars); and experimental (LRT) total eye aberration (light blue bars).

Figure 6 shows the linear correlations between total measured and simulated Zernike terms (astigmatism and high order aberrations) for the three eyes. There is a highly statistically significant correlation between the LRT-measured Zernike coefficients and those simulated from computer eyes model that incorporate all measured geometrical parameters (average slope = 0.82 ± 0.12; average coefficient of correlation R = 0.93 ± 0.05; p<0.0001). The correlations, although statistically significant, are lower between the LRT-measured Zernike and the anterior corneal Zernike terms (average slope = 0.69 ± 0.21; average coefficient of correlation R = 0.73 ± 0.05; p<0.0001); the LRT-measured Zernike and the entire cornea (anterior + posterior) corneal Zernike terms (average slope = 0.92 ± 0.23; average coefficient of correlation R = 0.88 ± 0.03; p<0.0001); and similar to the correlations between LRT-measured Zernike terms and simulated total aberrations from computer eye models assuming centered IOLs (average slope = 0.87 ± 0.1; average coefficient of correlation R = 0.94 ± 0.04; p<0.0001). Incorporating posterior cornea and IOL clearly improves the correlation, however including IOL tilt and decentration has only a minor impact (as also reported by Rosales and Marcos OE 2007 [14]).
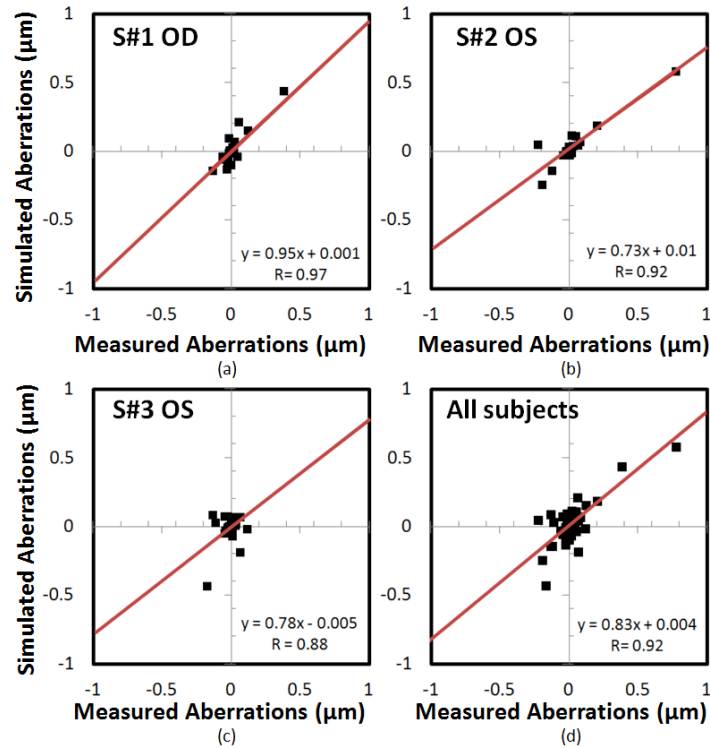
Fig. 6. Linear correlations between measured and simulated Zernike coefficients (astigmatism and 3rd and higher orders) in (a) S#1 OD; (b) S#2 OS; (c) S#3 OS; (d) combining data from the three subjects (72 points). Data are for 5-mm pupil diameters.

3.4 Corneal/IOL compensation

Comparison of the corneal aberrations to total aberrations (Fig. 5) allows evaluating compensatory effects between optical elements for different terms. We did not find a compensation of anterior corneal astigmatism by the posterior corneal astigmatism: in fact, total corneal astigmatism was higher than anterior corneal astigmatism in all three eyes (by 24.56% on average). In contrast, the posterior cornea consistently partially compensated anterior corneal spherical aberration (by 25.71%, on average) and coma (by 15.88%, on average). Consistently with aspheric IOL designs [6, 34], the IOLs compensated spherical aberration (by 72.14%, according to the simulations; and by 77.06%, by comparison of corneal and experimentally measured total aberrations) and coma (by 63.88% / 56.97%, on average).

3.5 Effect of IOL tilt and decentration on optical quality

The impact of the measured IOL tilt and decentration on optical aberrations appears to be minor, as revealed by the small differences in the simulated aberrations with the IOL aligned with the pupillary axis and those incorporating the real IOL tilt and decentration (0.04 μm for astigmatism and 0.04 μm for coma, on average in Fig. 5(a) and 5(d)). In fact, the presence of IOL tilt and decentration resulted in a slight decrease in the RMS in all three eyes (by 10.84% in RMS for astigmatism and higher order terms, on average). To further compare simulations and predictions, and analyze the effect of IOL tilt and decentration on optical quality, we computed the corresponding MTFs (radial profiles) for astigmatism and higher order terms (Fig. 7(a)) and 3rd and higher order aberrations (Fig. 7(b)), from wave aberrations simulated with centered IOLs, and IOL with real tilt/decentration, and from LRT-measurement.
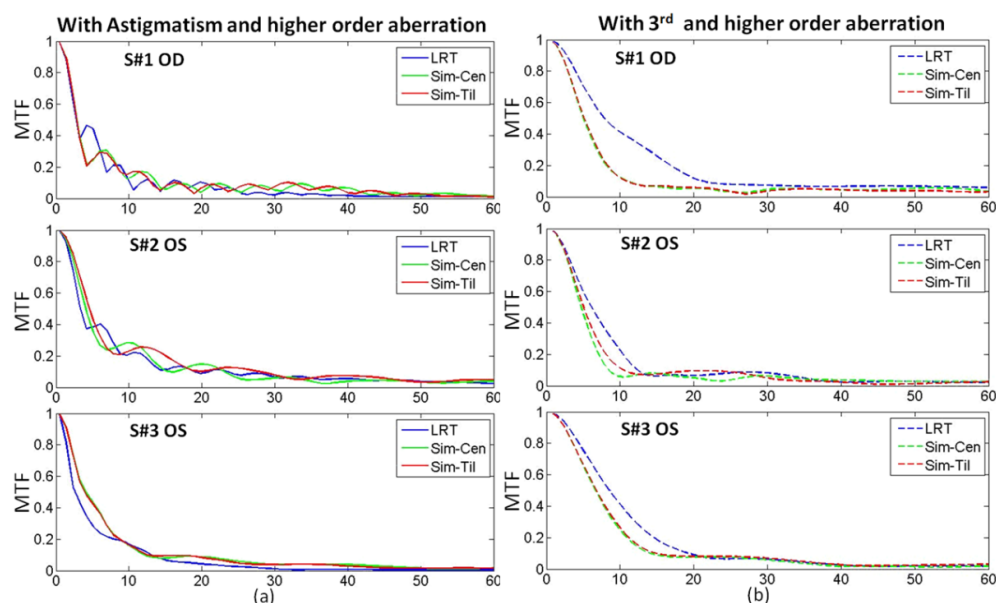
Fig. 7. (a) MTFs (radial profiles) for astigmatism and higher odder terms (b) MTFs (radial profiles) for 3rd and higher order aberrations, for LRT (blue lines), IOL with no tilt/decentration (green lines) and IOL with real tilt/decentration (purple lines). Data are for the three subjects, for 5-mm pupils.

The presence of IOL tilt/decentration improved optical quality (Visual Strehl) by 8.21% on average (Fig. 8).
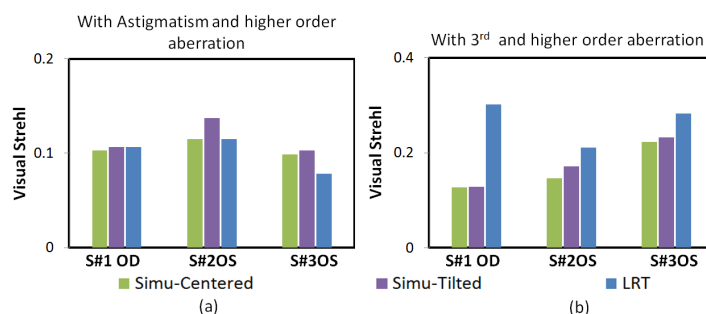

Fig. 8. (a) Corresponding Visual Strehl with Astigmatism and 3rd and higher order aberration (b) Corresponding Visual Strehl with 3rd and higher order aberration without Astigmatism (green bars present Simulation with IOL centered, purple bars present simulation with IOL tilt and decentration, blue bars present LRT).

4. Discussion

We have presented a customized computer eye model, using individual geometrical data in eyes with intraocular lenses obtained from quantitative 3D anterior segment Optical Coherence Tomography (OCT). The model predicted the wave aberrations measured in the same eyes with Laser Ray Tracing aberrometry within 0.12 μm accuracy (RMS for astigmatism and high order aberrations, for 5-mm pupils).

The geometrical quantification capabilities of the OCT and their accuracy, presented in previous works [16], allows exact ray tracing on computer eye models using this geometrical information, provided that the refractive indices of the cornea and intraocular media are known. Pseudophakic eyes are simpler than phakic eye models as the refractive index of the IOL material is known from the specifications of the manufacturer. Knowledge of the Abbe number of the IOL material would allow extrapolating the index of refraction from the visible to other wavelengths (i.e., IR typically used in wavefront

sensing). Nevertheless, chromatic effects are primarily of impact on defocus, and not high order aberrations [35, 36], which explains the good correspondence between LRT and simulated values, even if measurements were done in IR and simulations in green (i.e., the wavelength for which the indices of refraction of the IOL materials were available). In contrast, in phakic eyes the crystalline lens exhibits a patient/age-dependent Gradient Index Distribution [37, 38]. Computer eye models had been presented before [14, 15], using biometric information gathered from multiple devices (anterior cornea from Placido disk topography; tilt and decentration from Purkinje imaging apparatus; anterior chamber depth from slit lamp; axial length from low coherence interferometer). We found an average coefficient of correlation R = 0.93 between measured and simulated aberration. This compares with average coefficient of correlation R = 0.82 in Rosales and Marcos [14] and average coefficient of correlation R = 0.88 in Tabernero et al. reports [15].

Our study shows the capability of building computer eye models from information all obtained simultaneously with the same OCT system. Although our system did not have sufficient range to measure the axial length of the eye (and this information was obtained using low coherence interferometer on another device), different methods have been proposed to extent the range of OCT to allow for axial length measurements. These methods include a dual OCT system rapidly flipping between anterior and posterior segment imaging and MEM-based swept source OCT [39, 40].

The measurement of ocular aberrations in pseudophakic eyes allow assessment of the overall optical performance [5]. Customized eye models in combination with the actual measurements of ocular aberrations can be used to identify the relative importance of each factor. Our results in eyes implanted with aspheric IOLs show the compensation of part of the positive spherical aberration of the cornea with the IOL (by 66.43-85.89%). This is in agreement with the compensation reported with aspheric IOLs from different manufacturers (i.e. the Acrysof IQ (Alcon) by 66%) [34]. Very interestingly, as shown by Marcos et al. [34], aspheric IOLs also do appear to compensate for coma, particularly horizontal coma. We found a coma compensation of 59.43% with Asphina, and Marcos et al. [34] a compensation of 87% with Acrysof and Tecnis Aspheric IOLs. This compensation arises by a passive mechanism, from the combination of positive spherical aberration in the cornea and negative internally, and eye rotation, producing coma of opposite signs in the cornea and lens. Also in agreement with previous conclusions based on customized computer eye models [14], IOL tilt and decentration appear to play a minor role in the optical quality of the eye.

Previous customized computer eye models revealed a major role of the cornea in the ocular aberrations of the pseudophakic eyes, which also occurs in the three eyes of our study. However, generally those computer models did not incorporate real posterior corneal elevations (i.e. Rosales et al. [14] used a typical spherical posterior surface, Tabernero et al. [15] used a one-surfaced cornea). Several authors found a compensatory role of the anterior corneal astigmatism by the posterior cornea (14% in Dunne et al. [41] and 31% in Dubbelman [42]). Age-dependence changes of the anterior corneal astigmatism (i.e. astigmatism changes from with-the-rule to against-the-rule with age) may alter this balance. We did not find a lower total corneal astigmatism than that of the anterior corneal alone, suggesting no compensation in the three eyes of the study. Interestingly, the astigmatic axes of the anterior and posterior cornea do not appear aligned in all cases (Fig. 4, relative angles ranging from 2.3 to 56.7 degree). Axis misalignment of the anterior and posterior corneal astigmatism has been reported before [43] as well as misalignments in the astigmatic axes of the anterior and posterior crystalline lens surfaces [18, 44]. We did find consistent compensation by the posterior cornea of the anterior corneal spherical aberration and of anterior coma. The large differences in trefoil and tetrafoil might be explained by the larger fitting area of corneal surfaces in the 6-mm area while LRT was obtained for 5-mm pupil diameters.

The capability of OCT-based computer eye customized models to predict the measured aberrations post-operatively with a given implanted IOL opens the possibility to use those models as platforms to evaluate pre-operatively potential results with other IOLs, to optimize the selection of the IOL and improve optical outcomes. Given the

changes induced by small-incision cataract surgery on corneal aberrations, the model could be further refined by incorporating those induced aberrations to the pre-operative cornea to better reflect the post-operative corneal elevation maps. Marcos et al. [45] reported consistent significant changes in vertical astigmatism, trefoil and tetrafoil in patients in post-operative corneas of patients with superior 3.2-mm incisions. Neglecting intersubject and/or meridional variability in the corneal biomechanical response to the incision, these values could be incorporated on the appropriate Zernike terms in the model. Adjustments may be needed for different incision sizes for the clinical relevance for smaller incision sizes and physiological pupil diameters in probably minor.

OCT-based custom computer eye models are also applicable to the optimization of the IOL power calculation, using virtual ray tracing on these eyes. Ray tracing IOL power calculation overcomes many limitations of current IOL power selection techniques. These are typically based on regression models obtained for a large patient population, as opposed to the individualized approach based on customized eye models. Pre-operative measurements of anterior and posterior corneal surface overcome the limitations of the standard IOL power calculations which only make use of anterior corneal keratometry and the so-called keratometric index. Future analysis of the pre-operative anterior segment anatomy and crystalline lens from 3D OCT quantitative imaging will allow better predictions of the estimated lens position. Similarly to the comparisons between the measured and simulated high order aberrations addressed in the current study validations of the IOL power selections will involve comparisons of measured and predicted aberrometric defocus and/or refraction.

In summary, OCT-based customized computer eye models are excellent predictive tools of the optical quality in pseudophakic eyes, allow understanding the factors that contribute to optical degradation and hold promise to become a primary tool to optimize the selection of the IOL to be implanted in a cataract procedure.